

ARTICLE

OPEN



Temporal analog of Fabry-Pérot resonator via coherent population trapping

Ruihuan Fang ^{1,2,3}, Chengyin Han ^{1,3}, Xunda Jiang ^{1,2,3}, Yuxiang Qiu ^{1,2}, Yuanyuan Guo ^{1,2}, Minhua Zhao ^{1,2}, Jiahao Huang ¹✉, Bo Lu ¹✉ and Chaohong Lee ^{1,2}✉

Ramsey spectroscopy via coherent population trapping (CPT) is essential in precision measurements. The conventional CPT-Ramsey fringes contain numbers of almost identical oscillations and so that it is difficult to identify the central fringe. Here we experimentally demonstrate a temporal analog of Fabry-Pérot resonator via double- Λ CPT of laser-cooled ^{87}Rb atoms. By inserting a periodic CPT pulse train between the two CPT-Ramsey pulses, due to the constructive interference of spin coherence, the transmission spectrum appears as a comb of equidistant peaks in frequency domain and thus the central Ramsey fringe can be easily identified. From the five-level Bloch equations for our double- Λ system, we find that the multi-pulse CPT interference can be regarded as a temporal analog of Fabry-Pérot resonator. Because of the small amplitude difference between the two Landé g factors, each peak splits into two when the external magnetic field is not too weak. This splitting is exactly linear with the magnetic field strength and thus can be used for measuring a magnetic field without involving magneto-sensitive transitions.

npj Quantum Information (2021)7:143; <https://doi.org/10.1038/s41534-021-00479-y>

INTRODUCTION

Coherent population trapping (CPT)¹, a result of destructive quantum interference between different transition paths, is of great importance in quantum science and technology. CPT spectroscopy has been extensively employed in quantum engineering and quantum metrology, such as all-optical manipulation^{2–7}, atomic cooling⁸, atomic clocks^{9–13}, and atomic magnetometers^{14–17}. To narrow the CPT resonance linewidth, similar to the Ramsey interferometry in two-level systems¹⁸, one may implement CPT-Ramsey interferometry in which two CPT pulses are separated by an integration time of the dark state for a time duration T ^{19,20}. In a CPT-Ramsey interferometry, when the length of the second pulse is much smaller than the duration T , the fringe-width $\Delta\nu = 1/(2T)$ is independent of the CPT laser intensity and so that one may narrow the linewidth via increasing the time duration T ²¹. However, when the integration time T increases, it becomes difficult to identify the central CPT-Ramsey fringe from adjacent ones, as the adjacent-fringe amplitudes are almost equal to the central-fringe amplitude^{22,23}. Thus, it becomes very important to suppress the non-central fringes.

To suppress the non-central fringes, a widely used and highly efficient way is inserting a CPT pulse sequence between the two CPT-Ramsey pulses to implement multi-pulse CPT-Ramsey interference. By employing the techniques of multi-pulse phase-stepping^{24,25} or repeated query²³, the non-central fringes have been successfully suppressed. Similarly, high-contrast transparency comb²⁶ has been achieved via electromagnetically induced transparency multi-pulse interference²⁷. In analogous to multi-beam interference in spatial domain, multi-pulse interference in temporal domain has been proposed for two-level systems²⁸ and three-level Λ systems^{27,29}. The multi-pulse interferences, such as Carr-Purcell decoupling³⁰ and periodic dynamical decoupling³¹, have enabled versatile applications in quantum sensing³² from narrower spectral response, sideband suppression, to

environmental noise filtering. The existed experiments of multi-pulse CPT-Ramsey interference are almost performed under the σ - σ configuration, in which the two-photon transition occurs between states of the same magnetic quantum number. However, under the σ - σ configuration, atoms will gradually accumulate in a trap state that does not contribute ground-state coherence³³. To eliminate undesired atomic accumulations with no contributions to ground-state coherence, one may employ the lin||lin configuration^{33–37}. Under the lin||lin configuration, a bichromatic linear-polarized laser simultaneously couples two sets of ground states to a common set of excited state. Up to now, the multi-pulse CPT-Ramsey interference has never been demonstrated in experiments under the lin||lin configuration.

Usually, a CPT spectrum is relevant with the populations of ground states and their coherences. However, due to the absence of trap states in the lin||lin configuration, the populations of ground states are kept balanced. Therefore, the shapes of CPT spectrum are mainly determined by the spin coherence between ground states. This means that the CPT spectrum of the lin||lin configuration could manifest the spin coherence between ground states. By employing multiple CPT pulses, the spin coherence induced by different pulses will occur temporal interference.

In this work, based upon an ensemble of laser-cooled ^{87}Rb atoms under the lin||lin configuration, we experimentally and theoretically demonstrate that the temporal interference of spin coherence exactly corresponds to an optical Fabry-Pérot resonator (FPR)³⁸. We analytically obtain the transmission spectrum with arbitrary pulse length and pulse interval, and find that there is a mapping between the actions of CPT pulses and the reflection events of FPR. Through inserting a CPT pulse sequence between the two CPT-Ramsey pulses, similar to the constructive interference in a FPR, the central CPT-Ramsey fringe can be easily identified. Using identical pulses with equidistant interval, the transmission spectrum appears as a comb with multiple

¹Guangdong Provincial Key Laboratory of Quantum Metrology and Sensing & School of Physics and Astronomy, Sun Yat-Sen University (Zhuhai Campus), Zhuhai 519082, China.

²State Key Laboratory of Optoelectronic Materials and Technologies, Sun Yat-Sen University (Guangzhou Campus), Guangzhou 510275, China. ³These authors contributed equally: Ruihuan Fang, Chengyin Han and Xunda Jiang. ✉email: hjiahao@mail2.sysu.edu.cn; lubo3@mail.sysu.edu.cn; lichao2@mail.sysu.edu.cn

equidistant interference peaks and the distance between adjacent peaks is exactly the repeated frequency of the applied CPT pulses. Besides, we also observe peak splitting in such a multi-pulse CPT-Ramsey interference under a magnetic field. Due to the small difference of absolute value of the two Landé g factors of two ground hyperfine levels, each peak splits into two when magnetic field is not too weak³³. The central peak splitting is exactly linear with the magnetic field³⁹. In contrast, when the magnetic field is not large enough, this kind of splitting is hard to be observed via conventional CPT spectrum or conventional CPT-Ramsey interference. The multi-pulse CPT-Ramsey interference provides a useful tool for measuring a magnetic field without involving magneto-sensitive transitions.

RESULTS

Physical system

We consider the double- Λ system constructed by the D1 line of ^{87}Rb (see Fig. 1a). Under the lin||lin configuration, two CPT fields are linearly polarized to the same direction orthogonal to the applied magnetic field. A bichromatic field with frequencies of ω_a and ω_b simultaneously couples two sets of ground states $|F=1\rangle$ and $|F=2\rangle$ to a set of excited states $|F'=1\rangle$ in the D1 line of ^{87}Rb . In our system, $\Gamma=2\pi\times 5.746$ MHz is the excited-state decay rate, $\omega_{\text{hfs}}\approx 2\pi\times 6.83$ GHz is the hyperfine splitting of the ground state, and the two-photon detuning is $\delta=(\omega_a-\omega_b)-\omega_{\text{hfs}}$. There are a six-level and a five-level subsystems, which are labeled by black and red, respectively. In the presence of a bias magnetic field, the Zeeman sublevels are split with each other. Near $\delta=0$, there are four Λ structures. Two of the Λ structures couple $|F=1, m_F=0\rangle$ and $|F=2, m_F=0\rangle$ to excited states $|F'=1, m_F=\pm 1\rangle$ in the six-level subsystem. It is noteworthy that for $|F=1, m_F=0\rangle$ and $|F=2, m_F=0\rangle$, the spin coherence components induced by

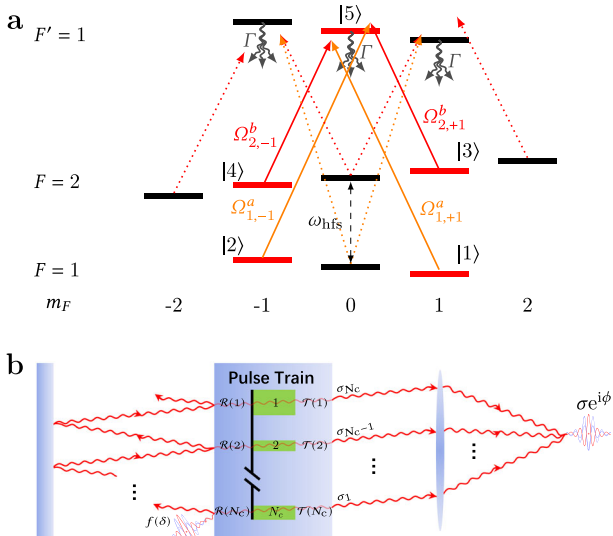


Fig. 1 Schematic diagram. **a** Energy levels of ^{87}Rb D1 line transitions under the lin||lin configuration. The black and red lines, respectively, denote two independent six-level and five-level subsystems. $\Omega_{1,\pm 1}^a$ and $\Omega_{2,\pm 1}^b$ are the Rabi frequencies of five-level subsystems, Γ is the decay rate from excited states to ground states, and ω_{hfs} is the zero-field hyperfine splitting of the ground state. $|1\rangle$, $|2\rangle$, $|3\rangle$, and $|4\rangle$ are four ground states of five-level subsystems. **b** The temporal analog of FPR, σ denotes the form of spin coherence, N_c is the total number of CPT pulses. The l -th CPT pulse, which corresponds to the (N_c-l+1) -th reflection event with the reflection coefficient $\mathcal{R}(l)$ and the transmission coefficient $\mathcal{T}(l)$, transmits σ_{N_c-l+1} , which is part of σ .

σ^+ and σ^- light components counteract each other, leading to the absence of two-photon resonance³³. The other two Λ structures couple $|1\rangle=|F=1, m_F=+1\rangle$ ($|2\rangle=|F=1, m_F=-1\rangle$) and $|4\rangle=|F=2, m_F=-1\rangle$ ($|3\rangle=|F=2, m_F=+1\rangle$) to the common excited state $|5\rangle=|F'=1, m_F=0\rangle$ in five-level subsystem and induces spin coherence relevant to the spectra. Thus, one can efficiently describe this double- Λ system via a 5-level model, although a complete description is an 11-level model (see more details in Supplementary Note 1). The Rabi frequencies for transitions from four ground states to the common excited state are respectively denoted by $\Omega_{1,\pm 1}^a$ and $\Omega_{2,\pm 1}^b$. Under the lin||lin configuration, the σ^+ and σ^- components of each light frequency have equal light intensity. According to the transition dipole moments (TDMs), we have $|\Omega_{1,+1}^a|=|\Omega_{1,-1}^a|$ and $|\Omega_{2,+1}^b|=|\Omega_{2,-1}^b|$. In general, the Rabi frequencies are complex numbers. However, in our five-level double- Λ model, the phase of four Rabi frequencies can be adjusted independently by selecting the initial phases of corresponding ground states. If one chooses appropriate phases of initial ground states, the Rabi frequencies could be satisfied as $\Omega_{1,\pm 1}^a=\Omega_1$ and $\Omega_{2,\pm 1}^b=\Omega_2$, with Ω_1 and Ω_2 being real hereafter⁴⁰.

By ignoring the population decay of ground states, the time evolution is governed by a Liouville equation^{41,42}

$$\frac{\partial \rho}{\partial t} = -\frac{i}{\hbar}(\hat{H}\rho - \rho\hat{H}^\dagger) + \dot{\rho}_{\text{trans-decay}} + \dot{\rho}_{\text{src}}, \quad (1)$$

with the density matrix $\rho = \sum_{j=1}^5 \sum_{i=1}^5 \rho_{ij} |i\rangle \langle j|$, the decoherence between ground states $\dot{\rho}_{\text{trans-decay}} = \sum_{j=2}^4 \sum_{i=1}^{j-1} (-\gamma_{ij} \rho_{ij} |i\rangle \langle j| + \text{h.c.})$ with the decoherence rates γ_{ij} obtained by fitting the experimental data with numerical simulation (see more details in Supplementary Note 7), and the population decay $\dot{\rho}_{\text{src}} = \sum_{i=1}^4 \frac{1}{4} \rho_{55} |i\rangle \langle i|$. If the ω_b is resonant to the single-photon transition $|F=2\rangle \rightarrow |F'=1\rangle$, the Hamiltonian of the double- Λ system reads

$$\begin{aligned} \hat{H} = & \hbar[(\delta + g_1 \frac{\mu_B}{\hbar} B_z) |1\rangle \langle 1| + (\delta - g_1 \frac{\mu_B}{\hbar} B_z) |2\rangle \langle 2| + g_2 \frac{\mu_B}{\hbar} B_z |3\rangle \langle 3| \\ & - g_2 \frac{\mu_B}{\hbar} B_z |4\rangle \langle 4| - \frac{i\Gamma}{2} |5\rangle \langle 5| + \frac{\Omega_1}{2} (|1\rangle \langle 5| + |2\rangle \langle 5| + \text{h.c.}) \\ & + \frac{\Omega_2}{2} (|3\rangle \langle 5| + |4\rangle \langle 5| + \text{h.c.})]. \end{aligned} \quad (2)$$

Here, B_z is the bias magnetic field along the light propagation direction, μ_B is the Bohr magneton, and $\{g_1, g_2\}$ are respectively the Landé g factors for ground states $F=1, 2$. For ^{87}Rb , g_1 and g_2 have a tiny different value but opposite signs; therefore, there are two magneto-insensitive transitions: $|1\rangle \leftrightarrow |4\rangle$ and $|2\rangle \leftrightarrow |3\rangle$. Experimentally, each density matrix element should be summed over the atoms contributing signals, i.e., $\rho_{ij} = \langle \hat{\rho}_{ij} \rangle$ ⁴³.

Mapping between multi-pulse CPT-Ramsey interferometry and FPR

Below we analyze the transmission spectra of CPT light in our double- Λ system. In experiments, the transmission of CPT light can be converted as the transmission signal (TS) via a photodetector (see “Methods”). The TS is proportional to $(1 - \rho_{55})$, i.e., the absorption is proportional to the excited-state population ρ_{55} . For simplicity, we do not consider degenerate Zeeman sublevels and set all four Rabi frequencies as the average Rabi frequency⁴⁴. To compare with the experimental observation, the average Rabi frequency can be given as $\Omega = \sqrt{(\Omega_1^2 + \Omega_2^2)/2}$ ⁴⁵. In the presence of a magnetic field, the resonant frequencies of magneto-sensitive two-photon transitions are away from that of the magneto-insensitive transitions. Moreover, noise of magnetic field will lead to rapid dephasing of the magneto-sensitive transitions⁴⁶. By comparing the experimental and numerical spectra, the dephasing rates of magneto-sensitive transitions $\{\Gamma_{12}, \Gamma_{13}, \Gamma_{24}, \Gamma_{34}\}$ are $2\pi \times 2$ kHz. Hence, the corresponding spin coherence elements

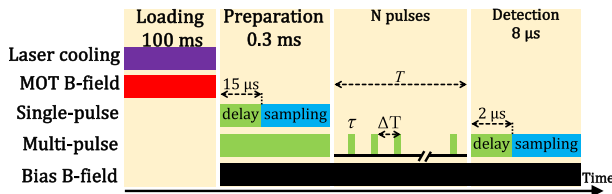


Fig. 2 Experimental timing sequence. A periodic CPT pulses with pulse length τ and pulse period ΔT is inserted between two CPT-Ramsey pulses respectively called as preparation and detection.

$\{\rho_{12}, \rho_{13}, \rho_{24}, \rho_{34}\}$ can be ignored near the magneto-insensitive two-photon resonance. Thus, using adiabatic elimination and resonant approximation⁴⁷

$$\rho_{55} = \frac{\Omega^2}{\Gamma^2} + \frac{2\Omega^2}{\Gamma^2} \operatorname{Re}(\rho_{14} + \rho_{23}). \quad (3)$$

Under the $\text{lin} \parallel \text{lin}$ configuration, for a weakly magnetic field, the two CPT resonances are nearly identical as $(|g_1| - |g_2|)\mu_B B_z \rightarrow 0$ ^{33,37}.

In a multi-pulse CPT-Ramsey interferometry of N_c pulses, the final excited-state population can be analytically given as (see more details in Supplementary Note 3)

$$\rho_{55} = \frac{\Omega^2}{\Gamma^2} + \frac{4\Omega^2}{\Gamma^2} \operatorname{Re}[\sigma(\delta)], \quad (4)$$

where the form of spin coherence is

$$\begin{aligned} \sigma(\delta) &= \sum_{l=1}^{N_c} \sigma_{N_c-l+1}(\delta) \\ &= \sum_{l=1}^{N_c} f(\delta) \left[\prod_{k=l+1}^{N_c} \mathcal{R}(k) \right] \mathcal{T}(l) e^{-i\delta \sum_{k=l+1}^{N_c} \Delta T(k)}, \end{aligned} \quad (5)$$

Exactly, the l -th pulse maps onto the $(N_c - l + 1)$ -th reflection event in an optical FPR (see Fig. 1b), in which $f(\delta) = -\frac{\Omega^2}{4\Gamma(\delta + \frac{\Omega^2}{\Gamma})}$ and the corresponding local reflection and transmission coefficients are respectively given as $\mathcal{R}(l) = v e^{-\frac{\Omega^2}{\Gamma} \tau(l)}$ and $\mathcal{T}(l) \equiv 1 - e^{-(\frac{\Omega^2}{\Gamma} + i\delta) \tau(l)}$, with the pulse length $\tau(l)$ and the pulse interval $\Delta T(l)$ for the l -th pulse. In our experiment, the pulse length and the pulse interval are chosen as $\tau(l) = \tau$ and $\Delta T(l) = \Delta T$, respectively. Therefore, $\sigma(\delta)$ can be simplified as

$$\sigma(\delta) = \sum_{l=1}^{N_c} f(\delta) \mathcal{R}^{(l-1)} \mathcal{T} e^{-i(l-1)\delta\Delta T}, \quad (6)$$

with the reflection coefficient $\mathcal{R} = e^{-\frac{\Omega^2}{\Gamma} \tau}$ and the transmission coefficient $\mathcal{T} = 1 - e^{-(\frac{\Omega^2}{\Gamma} + i\delta) \tau}$ constant. Obviously, the spin coherence (Eq. (6)) is analogous to the light transmission in an optical FPR.

Experimental demonstration

Now we present our experimental demonstration of the multi-pulse CPT-Ramsey interferometry with laser-cooled ^{87}Rb atoms (see “Methods”). Figure 2 describes the timing sequence of our experiment. To implement the multi-pulse CPT-Ramsey interferometry, about 10^7 ^{87}Rb atoms are cooled and trapped within a 100 ms loading period. Then the atoms are interrogated under free fall after turning off the magnetic field and the cooling laser beams of magnetic-optical trap (MOT). To ensure the MOT magnetic field decays to zero, the CPT beams and a bias magnetic field are simultaneously applied after 1 ms waiting time. The first CPT-Ramsey pulse with a duration of 0.3 ms is used to pump the atoms into the dark state and is here called as preparation. If no

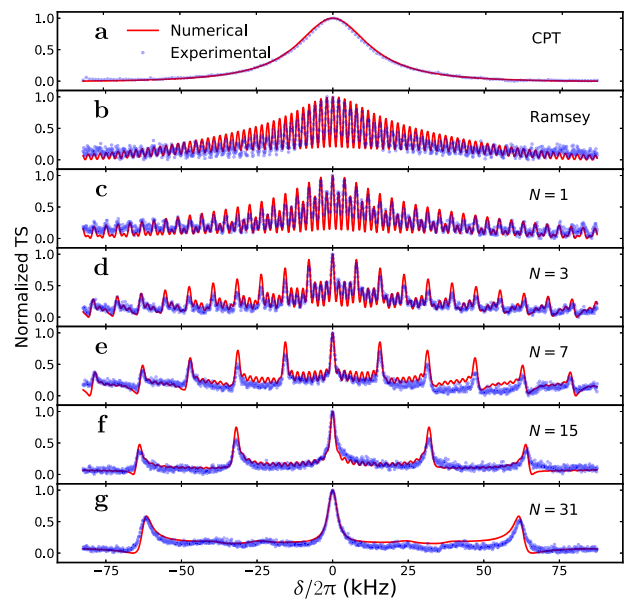


Fig. 3 Experimental transmission signals (TSs) for different schemes. **a** A Lorentz fitting of single-pulse CPT spectrum shows a full width at half maximum (FWHM) is 27 kHz. **b** Conventional CPT-Ramsey spectrum is obtained with an integration time of 0.5 ms. **c-g** Multi-pulse CPT-Ramsey spectra of N equidistant pulses with a length $\tau = 2 \mu\text{s}$ into the integration time of 0.5 ms.

following pulses are applied, a single-pulse CPT spectrum is obtained by averaging the collected TS of this pulse after a delay of 15 μs . By fitting the spectrum with a Lorentz shape, its full width at half maximum (FWHM) Δv is given as 27 kHz. In our experiment, the two components of bichromatic field have the same intensity. Considering the difference of TDMs, we can set $\Omega_1 = \Omega_2 / \sqrt{3}$. By comparing the spectrum with the numerical results of optical Bloch equations, the average Rabi frequency are estimated as $\Omega = 2\pi \times 0.28 \text{ MHz}$, which well agrees with the measured value through CPT light intensity of $I = 1.48 \text{ W m}^{-2}$. The CPT-Ramsey spectra are given by sampling the TS during the detection pulse after a delay of 2 μs . Without additional CPT pulses between the two CPT-Ramsey pulses, the central fringe in the conventional CPT-Ramsey spectrum is difficult to be distinguished from neighboring fringes (see Fig. 3b).

In our experiment, the multi-pulse CPT-Ramsey interferometry is performed by inserting N periodic CPT pulses (each pulse has a length of τ) between two CPT-Ramsey pulses as shown in Fig. 2. The minimum pulse length τ is limited to 1 μs , given by the precision of the controlled digital I/O devices. In Fig. 3c-g, we show the spectra for different pulse number N . Given the pulse length $\tau = 2 \mu\text{s}$ and the integration time $T = 0.5 \text{ ms}$, because of the constructive interference, high-contrast transmission peaks gradually appear when the pulse number N increases. According to Eq. (6), constructive interferences occur at $\delta/2\pi = m/\Delta T (m \in \mathbb{Z})$, which exactly give the resonance peaks in our experimental spectra (see Fig. 3). The distance between neighboring resonance peaks is equal to the free spectral range (FSR) $\Delta v_{\text{FSR}} = 1/\Delta T$ in analogous to FPR. For the conventional CPT-Ramsey, the FSR is 2 kHz and the FWHM is 1 kHz. Through inserting 31 periodic CPT pulses, the FSR increases 32 times to $\Delta v_{\text{FSR}} = 64 \text{ kHz}$, whereas the FWHM only increases 3.8 times to $\Delta v = 3.8 \text{ kHz}$. Due to the destructive interference, the background becomes more and more flat as the pulse number N increases, which makes the central fringe more distinguishable at a small expense of the linewidth broadening. In analogous to the optical FPR, the linewidth of periodic CPT pulses interference in steady-state

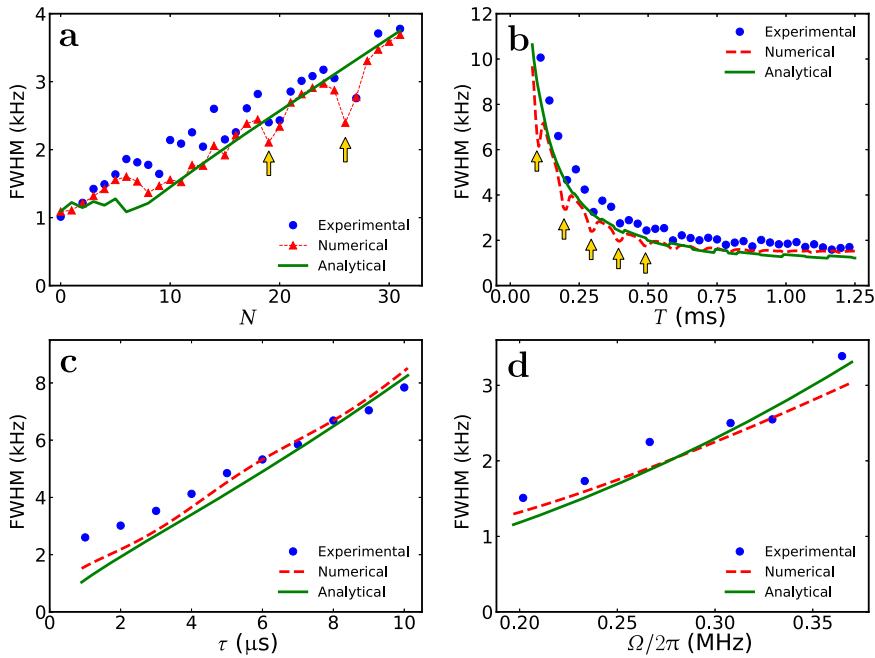


Fig. 4 FWHM aspects of multi-pulse CPT-Ramsey interferometry. **a** The FWHM vs. the pulse number N with $\Omega = 2\pi \times 0.28$ MHz, $T = 0.5$ ms, and $\tau = 2$ μ s. **b** The FWHM vs. the integration time T with $\Omega = 2\pi \times 0.28$ MHz, $N = 15$, and $\tau = 2$ μ s. **c** The FWHM vs. the pulse length τ with $\Omega = 2\pi \times 0.28$ MHz, $N = 15$, and $\Delta T = 0.031$ ms. **d** The FWHM vs. the average Rabi frequency Ω with $\tau = 2$ μ s, $N = 15$, and $\Delta T = 0.031$ ms. The bias magnetic field is chosen as $B_z = 0.116$ G and the yellow arrows label the exotic dips due to magneto-sensitive transitions.

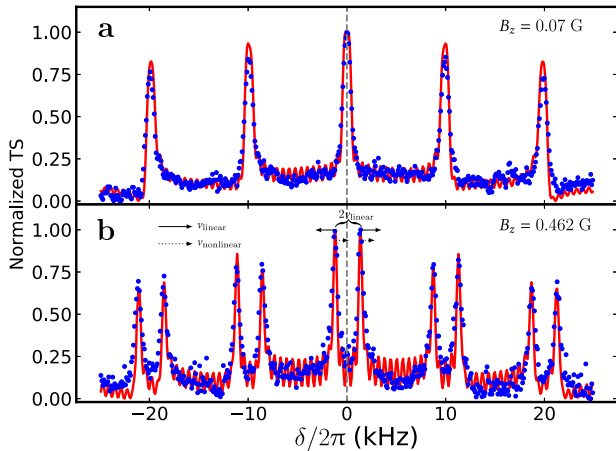


Fig. 5 Experimental TS (blue dots) under different bias magnetic fields B_z . In the experiments, 15 periodic CPT pulses with length $\tau = 2$ μ s are applied during the integration time $T = 1.6$ ms. The numerical results (red lines) is fitted with $\Omega = 2\pi \times 0.25$ MHz. The vertical gray dash line labels $\delta = 0$. **a** $B_z = 0.07$ G. **b** $B_z = 0.462$ G, the solid and dotted arrows respectively indicate the orientation of linear and nonlinear Zeeman shifts.

approach is $\Delta v = (2\Delta\nu_{\text{FSR}}/\pi) \arcsin[(1 - \sqrt{\mathcal{R}})/(2\sqrt[4]{\mathcal{R}})]$ ⁴⁸. Accordingly, the linewidth of multi-pulse CPT-Ramsey interference increases with the $\Delta\nu_{\text{FSR}}$, whereas it decreases as reflection coefficient \mathcal{R} increases.

To further show the power of our analytical results, we compare the experimental, numerical, and analytical linewidth. Figure 4 clearly shows that the experimental results are well consistent with the analytical and numerical ones. The linewidth increases with the pulse number N for a given integration time T , whereas it will decrease as the integration time T increases for a given pulse

number N . However, as labeled by the yellow arrows in Fig. 4a, b, there appear some exotic dips in the experimental and numerical results. These exotic dips are actually caused by a tiny contribution of magneto-sensitive transitions under the resonant condition $m/(B_z\Delta T) = 1.4$ MHz G⁻¹, (see more details in Supplementary Note 7). The linewidth increases with the pulse length τ and the average Rabi frequency Ω when the other parameters are fixed (see Fig. 4c, d). As the reflection coefficient $\mathcal{R} = e^{-\frac{\Omega^2}{T\tau}}$, this indicates that the linewidth increases as the reflection coefficient decrease.

Measuring static magnetic field via comparing magneto-insensitive transitions

The Landé g factors of two hyperfine ground states are $g_1 = (5g_i - g_J)/4$ for $F = 1$ and $g_2 = (3g_i + g_J)/4$ for $F = 2$, where $g_i = -0.0009951414(10)$ and $g_J = 2.00233113(20)$ are the Landé g factors for the nuclear and fine structures of $5^2S_{1/2}$. Usually, a static magnetic field should be measured via the Zeeman effects in a magnetic-sensitive transition. However, as the two involved Landé g factors have small amplitude difference, this difference will bring a frequency shift between the two magnetic-insensitive transitions $|1\rangle \leftrightarrow |4\rangle$ and $|2\rangle \leftrightarrow |3\rangle$; in principle, this frequency shift can be used to measure a static magnetic field. In the geomagnetic field (which is about 0.5 G), the frequency shift between the two magnetic-insensitive transitions is too small compared with the corresponding FWHM of CPT resonance and is hard to be detected by CPT-Ramsey fringes. Therefore, it is very difficult to be directly observed via single-pulse CPT spectra or conventional CPT-Ramsey spectra (see more details in Supplementary Note 6).

In contrast, by using the above multi-pulse CPT-Ramsey interferometry, the side peaks are suppressed compared with conventional CPT-Ramsey interferometry and thus the linewidth is decreased compared with single-pulse CPT spectra. In our experiment, in which the magnetic field is 0.462 G, the peaks of these transitions are exactly split (see Fig. 5b). According to the Breit-Rabi equation^{39,49}, the Zeeman shifts of the peaks v_{\pm} include

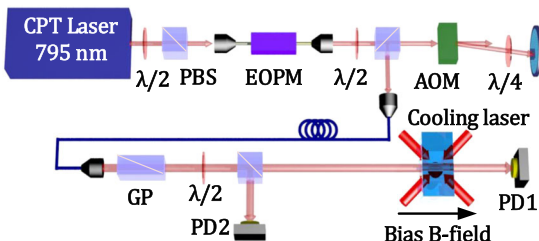


Fig. 6 Schematic diagram of our experimental apparatus. AOM: acousto-optic modulator, EOPM: electro-optic phase modulator, GP: Glan prism, PBS: polarization beam splitter, PD: photodetector.

a linear part v_{linear} and a nonlinear part $v_{\text{nonlinear}}$, i.e.,

$$v_{\pm} = \pm v_{\text{linear}} + v_{\text{nonlinear}} \quad (7)$$

The linear part $v_{\text{linear}} = \frac{\mu_B(|g_1|-|g_2|)}{2\pi\hbar} B_z$ is relevant with the amplitude difference of g_1 and g_2 . The nonlinear term is $v_{\text{nonlinear}} = \frac{\omega_{\text{hf}}}{4\pi} (\sqrt{1+x+x^2} + \sqrt{1-x+x^2} - 2)$ with $x = \mu_B \frac{(g_2-g_1)}{\hbar\omega_{\text{hf}}} B_z$. Given $B_z \sim 0.5$ G, the nonlinear part of the shift is only about 108 Hz, which displaces the center slightly. More importantly, as the nonlinear Zeeman effect is exactly canceled out, the splitting of the two magneto-insensitive peaks ($v_+ - v_-$) = $2v_{\text{linear}} = B_z \times 5568$ Hz G⁻¹ is exactly linear vs. the magnetic field (see Fig. 5b). Therefore, this peak splitting can be used for measuring a magnetic field without involving magneto-sensitive transitions.

DISCUSSION

In conclusion, we have experimentally demonstrated a multi-pulse CPT-Ramsey interference via laser-cooled ⁸⁷Rb atoms under the lin||lin configuration. The transmission spectrum appears as a high-contrast comb, in which a sequence of equidistant resonant peaks and non-resonant plains are respectively due to constructive and destructive interferences. We develop an analytical theory for the multi-pulse CPT-Ramsey interferometry based upon the five-level optical Bloch equations for our double- Λ CPT system, which can be regarded as a temporal analog of FPR. The temporal analog of FPR can be applied not only to the case of periodic identical pulses but also the pulse sequence with arbitrary pulse length and interval. It could also be extended to other systems, such as, coherent storage of photons in EIT⁵⁰ and coherent control of internal spin states in diamond defects⁶ or artificial atoms^{51–53}.

As the conventional CPT-Ramsey interference has several similar fringes in the center, it is difficult to identify the central peak around the resonant point, especially for cold atoms with low signal-to-noise ratio signals due to the limited number of trapped atoms. However, by inserting a periodic CPT pulse train, the fringes adjacent to the central peak can be eliminated to make the central peak more distinguishable. In portable clocks and low-cost clocks, stable locking is hard to establish. A distinguishable central peak is required to help relocking the clock quickly²⁵. In addition to identifying the central CPT-Ramsey fringe, our method could be directly used to measure clock transition frequency^{10–13} and static magnetic field^{14–17}. Despite the fact that spectrum FWHM will increase with the pulse number N , by reducing the pulse length τ and the Rabi frequency Ω (or increasing the integration time T), a smaller FWHM can still be obtained.

Besides, due to the small amplitude difference between the two Landé g factors, each peak splits into two when the external magnetic field is not too weak. This peak splitting can be used for measuring magnetic field without involving magneto-sensitive transitions. Although the sensitivity of central peak splitting is much smaller than the magneto-sensitive transitions, it is exactly linear with the magnetic field strength. Different from the magneto-sensitive transitions with second- and third-order

Zeeman shifts coefficients of 431 Hz G⁻² and ± 0.088 Hz G⁻³, the nonlinear Zeeman effect can be exactly canceled out in our scheme. Unlike our scheme, for the scheme using magneto-sensitive transitions, the systematic error caused by nonlinear Zeeman effects increases with the magnetic field strength. Roughly, the systematic error reaches 0.01%, 0.1%, and 0.375% when the magnetic field is 0.4, 4, and 15 G, respectively. By contrast, this systematic error is exactly canceled out in our scheme, which will be competitive in measuring relative strong magnetic fields. Moreover, as the central peak splitting is related to the nuclear Landé g factor g , it can be also used to measure g if B_z is known.

METHODS

Experimental setup

The schematic diagram of our experimental apparatus is shown in Fig. 6. Within an ultra-high vacuum cell with the pressure of 10^{-8} Pa, the ⁸⁷Rb atoms are cooled and trapped via a three-dimensional MOT, which is created by laser beams and a quadrupole magnetic field produced by a pair of magnetic coils. Two external cavity diode lasers (ECDLs) are used as the cooling and repumping lasers that are locked to the D2 cycling transition with a saturated absorption spectrum. To eliminate the stray magnetic field, three pairs of Helmholtz coils are used to cancel ambient magnetic fields. In addition, a pair of Helmholtz coil is used to apply a bias magnetic field aligned with the propagation direction of CPT laser beam to split the Zeeman sublevels.

The CPT laser source is provided by an ECDL locked to the $|F=2\rangle \leftrightarrow |F'=1\rangle$ transition of ⁸⁷Rb D1 line at 795 nm. The CPT beam is generated by modulating a single laser with a fiber-coupled electro-optic phase modulator (EOPM). The positive first-order sideband forms the Λ systems with the carrier. The 6.835 GHz modulated frequency matches the frequency splitting between the two hyperfine ground states. We set the powers of the first-order sidebands equal to the carrier signal by monitoring their intensities with an FPR. Following the EOPM, an acousto-optic modulator is used to generate the CPT pulse sequence. The modulated laser beams are coupled into a polarization maintaining fiber and collimated to an 8 mm-diameter beam after the fiber. A Glan prism is used to purify the polarization. Then, the CPT beam is equally separated into two beams by a half-wave plate and a polarization beam splitter. One beam is detected by the photodetector (PD2 in Fig. 6) as a normalization signal S_N to reduce the effect of intensity noise on the CPT signals. The other beam is sent to interrogate the cold atoms and collected on the CPT photodetector as S_T (PD1 in Fig. 6). The TSs are given by $S_{\text{TS}} = S_T/S_N$.

DATA AVAILABILITY

Data that support the figures within this paper and other findings of this study are available from the corresponding authors upon reasonable request.

CODE AVAILABILITY

The codes used for simulation and analysis will be made available to the interested reader upon reasonable request.

Received: 25 March 2021; Accepted: 1 September 2021;
Published online: 30 September 2021

REFERENCES

1. Gray, H. R., Whitley, R. M. & Stroud, C. R. Coherent trapping of atomic populations. *Opt. Lett.* **3**, 218–220 (1978).
2. Rogers, L. J. et al. All-optical initialization, readout, and coherent preparation of single silicon-vacancy spins in diamond. *Phys. Rev. Lett.* **113**, 263602 (2014).
3. Das, S., Liu, P., Grémaud, B. & Mukherjee, M. Magnetic coherent population trapping in single ion. *Phys. Rev. A* **97**, 033838 (2018).
4. Xia, K. et al. All-optical preparation of coherent dark states of a single rare earth ion spin in a crystal. *Phys. Rev. Lett.* **115**, 093602 (2015).
5. Santori, C. et al. Coherent population trapping of single spins in diamond under optical excitation. *Phys. Rev. Lett.* **97**, 247401 (2006).

6. Jamonneau, P., Hétet, G., Dréau, A., Roch, J.-F. & Jacques, V. Coherent population trapping of a single nuclear spin under ambient conditions. *Phys. Rev. Lett.* **116**, 043603 (2016).
7. Ni, K.-K. et al. A high phase-space-density gas of polar molecules. *Science* **322**, 231–235 (2008).
8. Aspect, A., Arimondo, E., Kaiser, R., Vansteenkiste, N. & Cohen-Tannoudji, C. Laser cooling below the one-photon recoil energy by velocity-selective coherent population trapping. *Phys. Rev. Lett.* **61**, 826–829 (1988).
9. Abdel Hafiz, M. et al. Symmetric autabalanced ramsey interrogation for high-performance coherent-population-trapping vapor-cell atomic clock. *Appl. Phys. Lett.* **112**, 244102 (2018).
10. Vanier, J. Atomic clocks based on coherent population trapping: a review. *Appl. Phys. B* **81**, 421–442 (2005).
11. Merimaa, M., Lindvall, T., Tittonen, I. & Ikonen, E. All-optical atomic clock based on coherent population trapping in ^{85}Rb . *J. Opt. Soc. Am. B* **20**, 273–279 (2003).
12. Yun, P. et al. High-performance coherent population trapping clock with polarization modulation. *Phys. Rev. Appl.* **7**, 014018 (2017).
13. Liu, X., Ivanov, E., Yudin, V. I., Kitching, J. & Donley, E. A. Low-drift coherent population trapping clock based on laser-cooled atoms and high-coherence excitation fields. *Phys. Rev. Appl.* **8**, 054001 (2017).
14. Scully, M. O. & Fleischhauer, M. High-sensitivity magnetometer based on index-enhanced media. *Phys. Rev. Lett.* **69**, 1360–1363 (1992).
15. Nagel, A. et al. Experimental realization of coherent dark-state magnetometers. *Europhys. Lett.* **44**, 31–36 (1998).
16. Schwindt, P. D. D. et al. Chip-scale atomic magnetometer. *Appl. Phys. Lett.* **85**, 6409–6411 (2004).
17. Tripathi, R. & Pati, G. S. Magnetic field measurement using peak-locked zeeman coherent population trapping resonance in Rubidium vapor. *IEEE Photon. J.* **11**, 1–10 (2019).
18. Ramsey, N. F. Successive oscillatory fields at radio to optical frequencies. *Appl. Phys. B* **60**, 85–88 (1995).
19. Thomas, J. E. et al. Observation of ramsey fringes using a stimulated, resonance raman transition in a sodium atomic beam. *Phys. Rev. Lett.* **48**, 867–870 (1982).
20. Zanon, T. et al. High contrast Ramsey fringes with coherent-population-trapping pulses in a double Lambda atomic system. *Phys. Rev. Lett.* **94**, 193002 (2005).
21. Abdel Hafiz, M. et al. A high-performance raman-ramsey cs vapor cell atomic clock. *J. Appl. Phys.* **121**, 104903 (2017).
22. Liu, X., Yudin, V. I., Taichenachev, A. V., Kitching, J. & Donley, E. A. High contrast dark resonances in a cold-atom clock probed with counterpropagating circularly polarized beams. *Appl. Phys. Lett.* **111**, 224102 (2017).
23. Warren, Z., Shahriar, M. S., Tripathi, R. & Pati, G. S. Pulsed coherent population trapping with repeated queries for producing single-peaked high contrast Ramsey interference. *J. Appl. Phys.* **123**, 053101 (2018).
24. Guerandel, S. et al. Raman–Ramsey interaction for coherent population trapping Cs clock. *IEEE Trans. Instrum. Meas.* **56**, 383–387 (2007).
25. Yun, P. et al. Multipulse Ramsey-CPT interference fringes for the ^{87}Rb clock transition. *Europhys. Lett.* **97**, 63004 (2012).
26. Yang, S.-J. et al. High-contrast transparency comb of the electromagnetically-induced-transparency memory. *Phys. Rev. A* **98**, 033802 (2018).
27. Nicolas, L. et al. Coherent population trapping with a controlled dissipation: applications in optical metrology. *New J. Phys.* **20**, 033007 (2018).
28. Akkermans, E. & Dunne, G. V. Ramsey fringes and time-domain multiple-slit interference from vacuum. *Phys. Rev. Lett.* **108**, 030401 (2012).
29. Pinel, O. et al. A mirrorless spinwave resonator. *Sci. Rep.* **5**, 17633 (2015).
30. Carr, H. Y. & Purcell, E. M. Effects of diffusion on free precession in nuclear magnetic resonance experiments. *Phys. Rev.* **94**, 630–638 (1954).
31. Viola, L. & Lloyd, S. Dynamical suppression of decoherence in two-state quantum systems. *Phys. Rev. A* **58**, 2733–2744 (1998).
32. Degen, C. L., Reinhard, F. & Cappellaro, P. Quantum sensing. *Rev. Mod. Phys.* **89**, 035002 (2017).
33. Taichenachev, A. V., Yudin, V. I., Velichansky, V. L. & Zibrov, S. A. On the unique properties of significantly increasing the contrast of dark resonances on the D1 line of ^{87}Rb . *JETP Lett.* **82**, 398–403 (2005).
34. Breschi, E. et al. Quantitative study of the destructive quantum-interference effect on coherent population trapping. *Phys. Rev. A* **79**, 063837 (2009).
35. Zibrov, S. A. et al. Coherent-population-trapping resonances with linearly polarized light for all-optical miniature atomic clocks. *Phys. Rev. A* **81**, 013833 (2010).
36. Mikhailov, E. E., Horrom, T., Belcher, N. & Novikova, I. Performance of a prototype atomic clock based on lin||lin coherent population trapping resonances in Rb atomic vapor. *J. Opt. Soc. Am. B* **27**, 417–422 (2010).
37. Esnault, F.-X. et al. Cold-atom double- Λ coherent population trapping clock. *Phys. Rev. A* **88**, 042120 (2013).
38. Renk, K. F. In *Basics of Laser Physics: Graduate Texts in Physics* (eds. Kurt, H. B. et al.) 2nd edn, Ch. 3 (Springer, 2012).
39. Knappe, S., Kemp, W., Affolderbach, C., Nagel, A. & Wynands, R. Splitting of coherent population-trapping resonances by the nuclear magnetic moment. *Phys. Rev. A* **61**, 012508 (1999).
40. Chen, X., Liu, I., Ruschhaupt, A., Guéry-Odelin, D. & Muga, J. G. Shortcut to adiabatic passage in two- and three-level atoms. *Phys. Rev. Lett.* **105**, 123003 (2010).
41. Warren, Z., Shahriar, M. S., Tripathi, R. & Pati, G. S. Experimental and theoretical comparison of different optical excitation schemes for a compact coherent population trapping rubidium vapor clock. *Metrologia* **54**, 418–431 (2017).
42. Shahriar, M. et al. Evolution of an N-level system via automated vectorization of the liouville equations and application to optically controlled polarization rotation. *J. Mod. Opt.* **61**, 351–367 (2014).
43. Gorshkov, A. V., André, A., Fleischhauer, M., Sørensen, A. S. & Lukin, M. D. Universal approach to optimal photon storage in atomic media. *Phys. Rev. Lett.* **98**, 123601 (2007).
44. Chen, Y.-C., Lin, C.-W. & Yu, I. A. Roles of degenerate zeeman levels in electromagnetically induced transparency. *Phys. Rev. A* **61**, 053805 (2000).
45. Hemmer, P. R., Shahriar, M. S., Natoli, V. D. & Ezekiel, S. Ac stark shifts in a two-zone Raman interaction. *J. Opt. Soc. Am. B* **6**, 1519–1528 (1989).
46. Baumgart, I., Cai, J.-M., Retzker, A., Plenio, M. & Wunderlich, C. Ultrasensitive magnetometer using a single atom. *Phys. Rev. Lett.* **116**, 240801 (2016).
47. Chuchelov, D. S. et al. Central ramsey fringe identification by means of an auxiliary optical field. *J. Appl. Phys.* **126**, 054503 (2019).
48. Ismail, N., Kores, C. C., Geskus, D. & Pollnau, M. Fabry-pérot resonator: spectral line shapes, generic and related airy distributions, linewidths, finesse, and performance at low or frequency-dependent reflectivity. *Opt. Express* **24**, 16366–16389 (2016).
49. Breit, G. & Rabi, I. I. Measurement of nuclear spin. *Phys. Rev.* **38**, 2082–2083 (1931).
50. Fleischhauer, M., Imamoglu, A. & Marangos, J. P. Electromagnetically induced transparency: optics in coherent media. *Rev. Mod. Phys.* **77**, 633–673 (2005).
51. Sánchez, R., López-Monís, C. & Platero, G. Coherent spin rotations in open driven double quantum dots. *Phys. Rev. B* **77**, 165312 (2008).
52. Donarini, A. et al. Coherent population trapping by dark state formation in a carbon nanotube quantum dot. *Nat. Commun.* **10**, 381 (2019).
53. Kelly, W. R. et al. Direct observation of coherent population trapping in a superconducting artificial atom. *Phys. Rev. Lett.* **104**, 163601 (2010).

ACKNOWLEDGEMENTS

This work is supported by the Key-Area Research and Development Program of Guangdong Province (2019B030330001), the National Natural Science Foundation of China (12025509 and 11874434), and the Science and Technology Program of Guangzhou (201904020024). J.H. is partially supported by the Guangzhou Science and Technology Projects (202002030459). B.L. is partially supported by the Guangdong Natural Science Foundation (2018A030313988) and the Guangzhou Science and Technology Projects (201804010497).

AUTHOR CONTRIBUTIONS

C.L., B.L., and J.H. conceived the project. C.H., X.J., and B.L. designed the experiment. R.F., C.H., and X.J. performed the experiments. R.F., J.H., and C.L. designed the theory. All authors discussed the results and contributed to compose and revise the manuscript. C.L. supervised the project. R.F., C.H., and X.J. contributed equally to this work.

COMPETING INTERESTS

The authors declare no competing interests.

ADDITIONAL INFORMATION

Supplementary information The online version contains supplementary material available at <https://doi.org/10.1038/s41534-021-00479-y>.

Correspondence and requests for materials should be addressed to Jiahao Huang, Bo Lu or Chaohong Lee.

Reprints and permission information is available at <http://www.nature.com/reprints>

Publisher's note Springer Nature remains neutral with regard to jurisdictional claims in published maps and institutional affiliations.



Open Access This article is licensed under a Creative Commons Attribution 4.0 International License, which permits use, sharing, adaptation, distribution and reproduction in any medium or format, as long as you give appropriate credit to the original author(s) and the source, provide a link to the Creative Commons license, and indicate if changes were made. The images or other third party material in this article are included in the article's Creative Commons license, unless indicated otherwise in a credit line to the material. If material is not included in the article's Creative Commons license and your intended use is not permitted by statutory regulation or exceeds the permitted use, you will need to obtain permission directly from the copyright holder. To view a copy of this license, visit <http://creativecommons.org/licenses/by/4.0/>.

© The Author(s) 2021